WILEY

RESEARCH ARTICLE

Active tugger line force control for single blade installation

Zhengru Ren[1,2,3] | **Zhiyu Jiang**[1,3] | **Zhen Gao**[1,2,3] | **Roger Skjetne**[1,2,3]

[1]Centre for Research-based Innovation of Marine Operations (SFI MOVE), Norwegian University of Science and Technology (NTNU), NO-7491 Trondheim, Norway

[2]Centre for Autonomous Marine Operations and Systems (AMOS), NTNU, NO-7491 Trondheim, Norway

[3]Department of Marine Technology, NTNU, NO-7491 Trondheim, Norway

Correspondence
Zhiyu Jiang, Centre for Research-based Innovation of Marine Operations, Norwegian University of Science and Technology, NO-7491 Trondheim, Norway.
Email: zhiyu.jiang@ntnu.no

Abstract

Single blade installation is one of the methods for installing large wind turbine blades at an offshore site. During this installation, each blade is lifted by the main crane from the deck of an installation vessel or a transportation barge with blade root approaching the hub. The blade root is then bolted to the hub. The final mating phase is critical and requires high precision. Tugger lines from the crane boom are connected to the suspended blade to reduce pendulum motions. The entire process is typically completed without active tugger line force control. Due to wind-induced blade loads, strict requirement on installation precision, and the limitations imposed by the lifting equipment, the single blade installation operations are subject to weather constraints. Therefore, developing techniques to reduce the blade motions and consequently shorten the installation time is desired. In this paper, an active control scheme is proposed to control the tugger line forces acting on a blade during the final installation stage before mating. A simplified three degree-of-freedom blade installation model is developed for the control design. An extended Kalman filter is used to estimate the blade motions and wind velocities. Feedback linearization and pole placement techniques are applied for the design of the controller. Simulations under turbulent wind conditions are conducted to verify the active control scheme, which effectively reduces the blade root motions in the wind direction.

KEYWORDS

extended kalman filter, feedback linearization, force control, pole placement, single blade installation, wind turbine

1 | INTRODUCTION

With increasing energy consumption and environmental concerns, renewable wind energy has received substantial scientific, societal, and industrial attention in recent years. Many countries plan to enlarge the share of wind energy in their national energy portfolio.[1] In 2016, wind energy accounted for 51% of all new energy installed capacity in the European Union.[2]

Because of land resource limitations and better wind quality, offshore wind turbines (OWTs) are becoming increasingly popular. At present, most offshore wind farms consist of wind turbines supported by monopiles, which are the most cost-effective type of support structure for shallow water.[3-7] However, the price of electricity from offshore wind can be approximately three to four times greater than electricity from onshore wind.[8] For an offshore wind farm project, capital expenditures (CapEx) and operational expenditures (OpEx) are the two main categories of the expenses. The assembly and installation cost is the third largest element in CapEx, accounting for 11.6%.[8] Offshore installations, including lifting and mating operations, are expensive. Because of the limitations of lifting and monitoring equipment, spending time waiting for the right weather window is not uncommon.

Selecting the suitable installation method for OWTs is often a trade-off among several aspects, such as onshore and offshore assembly costs, crane capacity, and deck usage of the transportation vessel. Different installation strategies exist, with varying numbers of pre-assembled components and offshore lifts. For example, if the rotor and all three blades are assembled onshore, then only one offshore lift is required for the rotor assembly, without the need for individual blade lifts.[9] As the rotor diameters of the biggest wind turbines begin to reach 180 m, lifting an entire rotor assembly offshore may face more challenges in addition to transportation issues. Large and high cranes have to be used.

Single blade installation is one of the alternatives for installing wind turbine blades at an offshore site. In this approach, one blade is lifted by the main crane from the deck of an installation vessel or a transportation barge and attached to the nacelle on the top of the tower. Tugger lines are used

to connect the suspended blade to the crane boom to reduce pendulum motions, typically without any active control. Single blade installation allows for the selection of a wider range of installation vessels with lower crane capacity. The deck space is more efficiently used, and a crane vessel can carry more turbine components in a single trip. Nevertheless, single blade installation requires more offshore lifts than the assembled rotor approach, and it is limited to a mean wind speed[10] of 8 to 12 m/s. Recently, both the research community and industry have made efforts to understand the physics of and to make improvements to the state-of-the-art single blade installations. The aerodynamics and aeroelastic behavior of a single blade at standstill are studied in other studies.[10-13] In Jiang et al,[14] the motion characteristics of a blade installation model are identified, and the critical parameters that influence the final blade installation stage are investigated. Meanwhile, specialized commercial products, such as LT575 Blade Dragon,[15] allow single blade installations to be conducted under higher wind speeds. Another example is the Boom Lock technology,[16] which reduces the blade motion and expands the operational limits.

In addition to the aforementioned tools, using automatic control to assist single blade installation is of interest. Successful applications of automatic control are familiar in the fields of marine operations and wind turbine operations. Traditionally, marine operations are heavily dependent on human interactions. With the advancements in automatic control, many operations can be performed with increased efficiency and reliability. In the field of ship-mounted crane operations alone, various control strategies have been applied to reduce the motions of suspended cargoes,[17-20] to reduce the roll motion,[21] and to facilitate moonpool operations.[22,23] For wind turbines, studies have primarily focused on the operating conditions. Control strategies are developed concerning voltage control,[24] generator speed regulation,[25] and load reduction.[26] However, to the authors' knowledge, no active control scheme has been applied to regulate the tugger line forces for blade installation purposes.

In this paper, a closed-loop control scheme for single blade installation is proposed, which includes an extended Kalman filter (EKF) and a feedback linearization proportional-integral-derivative (PID) controller. The active controller reduces the blade motions in the assumed scenarios and can potentially be used to expedite the installation process. The remainder of this paper is structured as follows. The system description and problem formulation are presented in Section 2. Additionally, a simplified control design model (CDM) with the blade motion described by three degrees of freedom (DOFs) is introduced for designing the observer and the controller. A simulation verification model (SVM) with a 6DOF blade is also introduced to verify the closed-loop performance. In Section 3, an EKF is designed to filter the measurement noise and to estimate the unknown states, while the feedback linearization and pole placement techniques are applied in the control design. Section 4 presents the verification of the control scheme using both the CDM and the SVM. A set of comparative studies are conducted to prove the active controller performance. Section 5 presents conclusions and recommendations for future studies.

Notations: In this paper, scalars, vectors, and matrices are denoted with normal lowercase letters, bold lowercase letters, and bold capital letters, respectively.

2 | PROBLEM FORMULATION

2.1 | Description of the installation procedure

The installation of an offshore monopile-type wind turbine can be divided into several stages. The monopile is first hammered into the seabed, followed by assembly of the transition piece, tower, nacelle, and blades. Three lifts are involved for the blades if the single blade installation technique is applied. Before the blade installation begins, the hub is rotated to a horizontal position for wind turbines with a conventional gear transmission. Then, the blade is seized by a yoke at its center of mass and lifted to the hub height by a crane vessel from the deck. At the final installation stage, the blade root motions are closely monitored using an onboard motion capture device.[27] If the motions are within the allowable limits, then the mating process follows. Figure 1 illustrates a typical mating phase between the blade and hub. Tugger lines are used to constrain the blade motions. When the guide pins on the blade root have entered the flange holes on the hub, the mating process is finished. Then, manual work is involved to bolt the blade onto the hub, followed by retraction of the lifting gear. A detailed description of the procedure can be found in Jiang et al.[14]

The main wind direction is supposed to be constant. Two reference frames with right-hand coordinates are defined in the following:

- Global frame $\{G\}$: The origin O_g is placed at the mean water level with the x-axis pointing in the constant main wind direction, the z-axis pointing downward, and the y-axis according to the right hand rule. The rotations about the x-, y-, and z-axes are named roll (ϕ), pitch (θ), and yaw (ψ), respectively.
- Blade body-fixed frame $\{B\}$: The origin O_b is located at the blade center of gravity (COG). The y^b-axis points in the spanwise direction, from the root to the tip. The z^b-axis points downward. The planar translational velocity in the body-fixed frame and the rotational velocity in yaw are denoted by u, v, and r, respectively.

2.2 | Control design model

To facilitate the design of an observer algorithm and a control law, we use a simplified CDM to describe the blade installation system. The following fundamental assumptions are made in the analysis:

1. The position of the crane tip $[x_p, y_p, z_p]^\top$ remains constant. Without loss of generality, we assume that $[x_p, y_p]^\top = [0, 0]^\top$.
2. Only the three planar motions are considered, ie, surge (x), sway (y), and yaw (ψ).
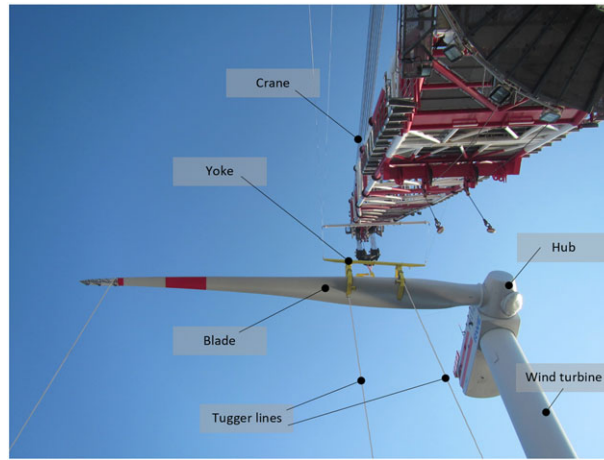
FIGURE 1 Illustration of the mating phase during a single blade installation. (Image source: RWE GmbH[28]) [Colour figure can be viewed at wileyonlinelibrary.com]

3. The blade yaw angular velocity $\dot{\psi}$ is small.
4. The blade motions in different DOFs at COG are independent, but the resulting translational motions at the blade root are also dependent on the yaw motion.

Based on these assumptions, a decoupled 3DOF single blade installation model can be expressed as follows:

$$\dot{\eta} = R v, \tag{1a}$$

$$\dot{b} = -\frac{1}{T_b} b + w_b, \tag{1b}$$

$$M \dot{v} = R^\top (g + b + Bu) + \tau_w, \tag{1c}$$

$$\dot{U}_w = -\frac{1}{T_w} U_w + w_w, \tag{1d}$$

where $\eta = [x, y, \psi]^\top \in \mathbb{R}^2 \times \mathbb{S}$ denotes the position and orientation of the blade COG in the global frame, $v = [u, v, r]^\top \in \mathbb{R}^3$ includes the linear velocity and the updating rate of the Euler angle in the body-fixed frame, and $U_w \in \mathbb{R}$ is the mean wind speed. R is the transformation matrix from the body-fixed frame to the global frame, and it is given by the following:

$$R(\psi) = \begin{bmatrix} \cos\psi & -\sin\psi & 0 \\ \sin\psi & \cos\psi & 0 \\ 0 & 0 & 1 \end{bmatrix}. \tag{2}$$

Note that the rotation matrix R in the horizontal plane satisfies

$$R^{-1} = R^\top, \quad \dot{R} = RS(r), \quad \text{where} \quad S(r) = \begin{bmatrix} 0 & -r & 0 \\ r & 0 & 0 \\ 0 & 0 & 0 \end{bmatrix}. \tag{3}$$

$M = \operatorname{diag}(m, m, I_b)$ denotes the mass matrix of the system where $m = m_b + m_h + m_y$ is the total mass combining the blade, hook, and yoke masses and I_b is the blade's moment of inertia.

In Equation 1c, $g = [-\frac{mg}{l}(x - x_p), -\frac{mg}{l}(y - y_p), 0]^\top$ represents the gravity-induced restoring force where l is the distance between the crane tip and the blade COG. $u = [u_1, u_2]^\top \in \mathbb{R}^2$ is the control input vector, where u_1 and u_2 are the tugger line horizontal force inputs. These can be both positive and negative because of pretension. The pretension is generated by gravity due to the initial displacement of the blade. The control allocation matrix B is used to transfer the tugger line force inputs to the generalized control force in the global frame. It is given by

$$B = \begin{bmatrix} -1 & -1 \\ 0 & 0 \\ -r_{t1}\cos\psi & r_{t2}\cos\psi \end{bmatrix}, \tag{4}$$

where $r_{t1} > 0$ and $r_{t2} > 0$ are the moment arms of the tugger line forces u_1 and u_2 with respect to the COG.

$\boldsymbol{\tau}_w$ represents the wind load acting on the blade COG in the body-fixed frame. The mean wind velocity in the global frame is assumed to be $\boldsymbol{u}_w = [U_w, 0, 0]^\top$. After coordinate transformation by the yaw angle ψ, the wind velocity in the body-fixed frame is $\boldsymbol{u}_w^b = [U_w \cos\psi, -U_w \sin\psi, 0]^\top$. The wind induced-force in the body-fixed frame at an airfoil segment depends on the inflow velocity relative to the blade segment at y^b, given by $\boldsymbol{u}_{wr}^b(y^b) = \boldsymbol{u}_w^b - \boldsymbol{u}_b^b(y^b)$, where $\boldsymbol{u}_b^b(y^b)$ is the velocity at the blade segment center of pressure at y^b. It is practical to assume that the blade motion is small and negligible compared with the mean wind speed. Hence, $\boldsymbol{u}_w^b$ is instead used directly to calculate the induced wind force. It should also be noted that the wind-induced force in the y^b-direction is negligible compared with the force in x^b-direction and the moment in yaw. Thus, we assume that the wind-induced load in sway (y^b-axis) is zero, according to the cross-flow principle. To sum up, the simplified wind-induced load for the CDM is then given by

$$\boldsymbol{\tau}_w = \begin{bmatrix} f_{wx} \\ f_{wy} \\ m_w \end{bmatrix} = \begin{bmatrix} aU_w^2\cos^2\psi \\ 0 \\ bU_w^2\cos^2\psi \end{bmatrix}, \tag{5}$$

where $a = \sum_i a_i = \sum_i \frac{1}{2}\rho_{air}\bar{C}_d(t_i)\sin^2(\alpha_i)A_i$ and $b = \sum_i a_i r_i$ according to a segmentation of the blade into n elements. Here, ρ_{air} refers to the air density, $\bar{C}_d(t_i)$ is the aerodynamic drag coefficient with respect to the relative thickness t_i of the ith segment center, and α_i is the angle of attack that depends on the pitch θ and aerodynamic twist. $A_i = (r_{i+1} - r_i)C_i$ is the wing area, where C_i is the chord length, and r_i is the distance from the center of the ith segment to the COG. The cross-flow principle[10] is applied to calculate the wind loads on the blade, and interested readers are referred to Ren et al[29] for a verification using the HAWC2[30] numerical model. Simulation results in Ren et al[29] has also proven the feasibility of the assumptions for Equation 5.

A state vector $\boldsymbol{b} = [b_1, b_2, b_3]^\top \in \mathbb{R}^3$ is used in the observer to estimate the forces and moments biases in $\{B\}$ caused by the pretension, model uncertainty, environmental disturbance, etc. Elements in vector $\boldsymbol{b}$ are assumed to be primarily due to the variation in the blade pitch, as illustrated in Figure 2. After exerting the pretension on the tugger lines, the blade moves in the opposite direction of the incoming wind and becomes inclined with respect to its original position. The inclination affects the blade pitch angle and the airfoil angle of attack along the blade. In addition, the model uncertainty also has an impact on $\boldsymbol{b}$. For example, the wind-induced load $\boldsymbol{\tau}_w$ in Equation 5 is a simplified approximation since the blade aerodynamics is very complex in a turbulent wind field.[31,32] Therefore, the deviation of the total wind-induced loads in different DOFs is modeled as a slowly varying Markov model in a vector form, Equation 1b, where $\boldsymbol{T}_b = \text{diag}\{T_{b1}, T_{b2}, T_{b3}\}$ is a constant diagonal matrix, with parameters $T_{b1}, T_{b2}, T_{b3} > 0$ to be tuned during the observer design stage. The process disturbance $\boldsymbol{w}_b = [w_{b1}, w_{b2}, w_{b3}]^\top \in \mathbb{R}^3$ and the wind speed disturbance $w_w \in \mathbb{R}$ are Gaussian white noise processes. The wind speed disturbance is used to account for the location-dependent wind since an anemometer is generally installed on the yoke; it is only able to measure the wind speed of one location.

The measurement equation is given by

$$\boldsymbol{y} = \boldsymbol{Hx} + \boldsymbol{v}, \tag{6}$$

where $\boldsymbol{x} = [\boldsymbol{\eta}^\top, \boldsymbol{b}^\top, \boldsymbol{v}^\top, U_w]^\top \in \mathbb{R}^{10}$ is the state vector, $\boldsymbol{y} = [x, y, \psi, U_w]^\top \in \mathbb{R}^4$ is the sensor measurement vector containing the position of the blade COG and wind speed measurement from the anemometer, and $\boldsymbol{v} = [v_x, v_y, v_\psi, v_{U_w}]^\top \in \mathbb{R}^4$ is the Gaussian sensor white noise vector. The output matrix $\boldsymbol{H}$ is given in Appendix A.

2.3 | Simulation verification model

Rather than the simplified CDM that addresses the horizontal problem, an SVM in full 6DOF should be used to verify the controller performance. The SVM considers the coupling of DOFs within a body and captures more physics of the system. Table 1 highlights the differences between the SVM and the CDM. In the SVM, the blade is modeled as a 6DOF rigid body, and the lift wire, slings, and tugger lines are all modeled as linear tensile
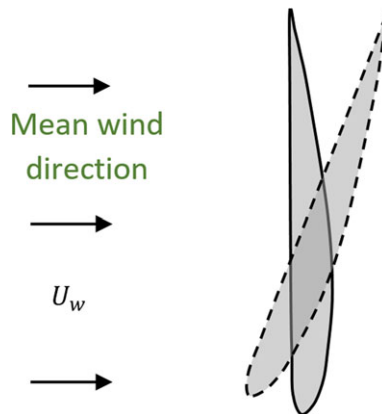
FIGURE 2 Illustration of the variation in the blade pitch angle (solid line represents the assumed orientation, and dashed line represents a possible orientation) [Colour figure can be viewed at wileyonlinelibrary.com]

springs. The hook is modeled as a rigid point with three DOFs. Moreover, the lift wire and tugger lines are assumed to be rigidly fixed to the crane tip and crane boom, respectively.

Ignoring the blade flexibility, the present blade model in SVM does not fully represent the aerodynamic loads acting on the blade. Figure 3 gives a comparison of the numerical models on the aerodynamic force and moment distribution along the length of the NREL 5-MW blade. For the rigid-blade case, there is a good agreement between the SVM model and the HAWC2 model; refer to Ren et al.[29] For the flexible-blade case, only HAWC2 is used, and the distributed lift forces experience harmonic oscillations; the deviations from the rigid-blade results become greater at the blade tip which has more flexibility. Unlike a blade on an operating wind turbine, a blade during offshore installations experiences no cyclic motions and has low moving speed, and usually the inboard part of the blade (radius<20 m) is more heavily loaded. Hence, the blade flexibility is expected to have less impact on the integrated aerodynamic forces and moments. As the focus of this paper is on the development of control methods, we use the rigid-blade model in estimation of the aerodynamic loading for the sake of simplification, ie, Equation 5.

2.3.1 | Actuator dynamics

In the SVM, a sophisticated actuator model depends on industrial winch products[33] suitable for such an operation, but this is beyond the scope of this work. The ability of the tugger lines to supply the desired forces fast enough, dependent on the actuator characteristics. Due to the dynamic responses and physical limitations of the winches, the control signal cannot reach any desired values or change at any desired rate. Additionally, the

TABLE 1 Components of the simulation verification model and the control design model

Components	Simulation verification model	Control design model
Lift wire	Yes	Yes
Hook	3DOF	No
Slings	Yes	No
Blade	6DOF	3DOF
Tugger lines	Yes	Yes
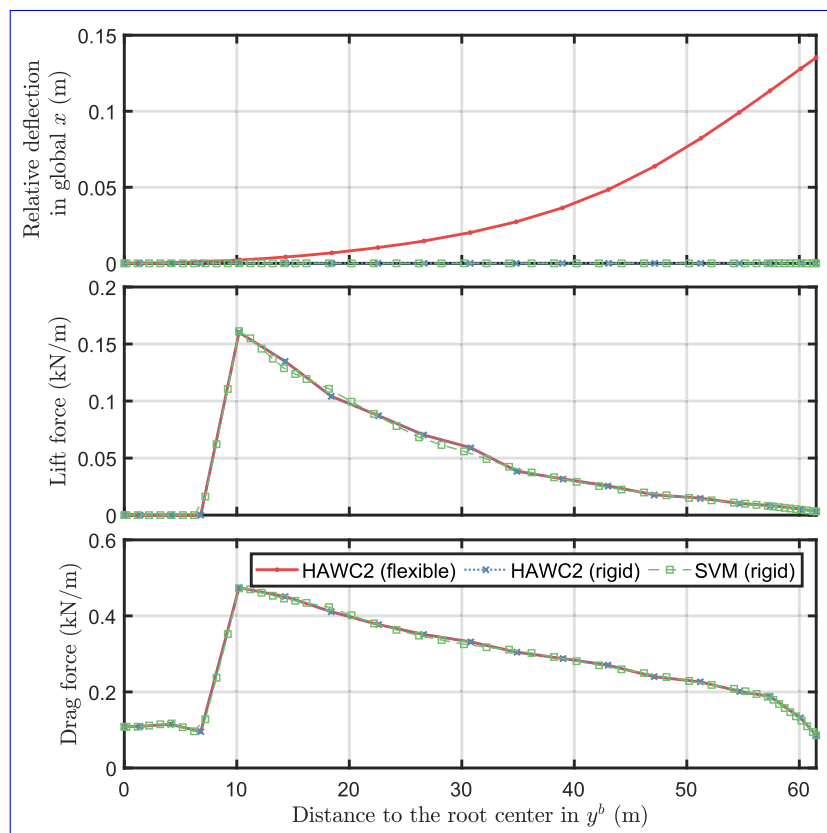
FIGURE 3 Comparison of the aerodynamic load distribution on a blade fixed at the root ($\theta = 90$ deg and $U_w = 10$ m/s) [Colour figure can be viewed at wileyonlinelibrary.com]
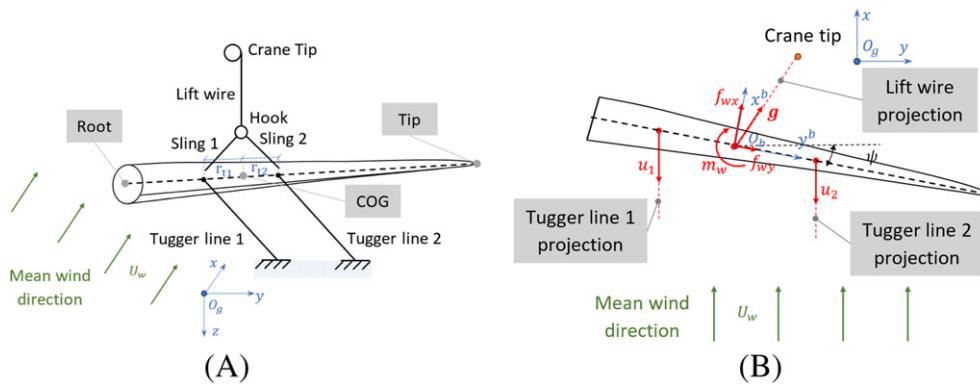
FIGURE 4 Scenario of the final installation stage of a blade prior to mating. A, 3-D view and B, 2-D projection in the horizontal plane. The red arrows stand for forces and moment; the blue lines denote the coordinate systems [Colour figure can be viewed at wileyonlinelibrary.com]

other ends of the ropes move with the connecting points on the yoke-blade structure, which makes the tension control process more complex. In this study, the actuator process is simplified as a stable first-order dynamics,[34] expressed in the frequency domain by

$$\frac{u_i(s)}{u_{cmd,i}(s)} = \frac{T_{iu}}{s + T_{iu}}, \quad i \in \{1, 2\}, \tag{7}$$

where $1/T_{iu}$ is the time constant of the lowpass filter which influences the speed of convergence, and $u_{cmd,i}$ is the control input command signal from the proposed controller described in Section 3.3.

2.4 | Problem statement

Figure 4A illustrates a typical scenario prior to the mating phase. The leading edge of the blade faces downward with a 90-deg pitch angle. This blade orientation does not have minimal loading, but it is often adopted in practice due to the concerns for transportation and loading predictability when wind direction changes.[13] One lift wire is used to rigidly connect the hook and crane tip, and two slings are used to connect the hook and yoke. Two horizontal tugger lines are connected to the blade with arm lengths of r_{t1} and r_{t2} relative to the blade COG.

Figure 4B presents a top view of the scenario. In the figure, g is the restoring force caused by the blade gravity, u_1 and u_2 are the horizontal components of the tugger line forces. The global x-direction is critical for this configuration because large loads are exerted on the blade system. The turbulent wind continuously affects the motion of the blade. The control objective is therefore to stabilize the blade in the main wind direction, in particular the blade root position, by controlling the force inputs, u_1 and u_2, assuming these are control inputs (and disregarding the actuator dynamics, which afterwords are individually controlled through a control allocation method).

To achieve this in practice, there is a need to apply a pretension by moving the blade with an initial offset before the mating operation. To move the blade to a desired setpoint r_d with required pretension, a reference filter should be used to generate a smooth trajectory to avoid a sudden step change of the setpoint r_d. After reaching r_d and desired orientation, these are kept constant and the blade should be kept stable. The control objective is thus to control the blade COG to track the desired position and orientation given by the reference filter. The ultimate goal is to reduce the motion of the root center in order to ensure a successful mating operation.

3 | DEVELOPMENT OF THE CONTROL ALGORITHM

3.1 | System overview

In this work, the observer and the controller are designed independently by assuming the separation principle.[35] The block diagram of the control scheme is presented in Figure 5. At each time instant, an EKF receives the noisy measurements y from sensors to estimate the blade position and orientation $\hat{\eta}$, the blade velocity $\hat{v}$, the wind velocity $\hat{U}_w$, and the bias compensation term $\hat{b}$. When the controller is turned on at time t_0, the EKF provides the initial value for the reference model and controller. A reference module is applied to generate smooth trajectories of the real-time desired position and velocity, denoted by η_d and v_d, to the preset setpoint where the blade is stabilized. All estimates and reference signal are fed back into the feedback controller. The controller calculates the corresponding tension input u to the two tugger lines according to the error between the estimated values and the desired trajectory, as well as some feedforward compensation of the estimated wind and bias loads.

3.2 | Extended Kalman filter

Because the sensors only measure the noisy blade COG position and wind velocity, the blade velocity at the COG is obtained from an observer. A model-based observer not only filters the measurement noise but also estimates the unmeasured states, ideally with no phase lag. An EKF with
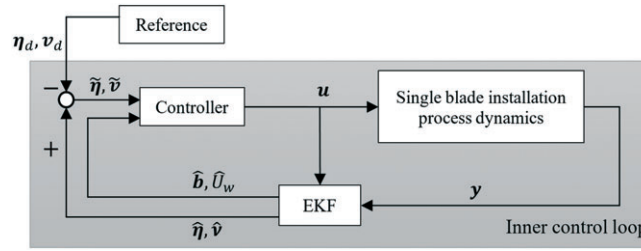
FIGURE 5 Block diagram of the active control scheme for single blade installation. The hat operator (ˆ) denotes the estimation. The tilde (˜) indicates the error between the estimated and desired value (eg, $\tilde{\eta} = \hat{\eta} - \eta_d$)

discrete measurements is used to estimate the states of the simplified system modeled by Equation 1. A continuous model evaluated and measured at discrete time instants is expressed as follows:

$$\dot{x}(t_k) = f(x(t_k), u(t_k)) + Ew(t_k), \tag{8a}$$

$$z_k = Hx(t_k) + v(t_k), \tag{8b}$$

where x is the state variables to be estimated, u is the force input vector, z_k refers to the sampled measurement vector at time t_k, w is the white-noise process presenting system disturbances, v is the Gaussian white noise of the sensor measurements, and f and H correspond to the state equation vector and the output matrix, respectively. The subscript k refers to the kth time step t_k. The time step length is $h = t_k - t_{k-1}$, and the vector elements are $x = [x, y, \psi, b_1, b_2, b_3, u, v, r, U_w]^\top$, $u = [u_1, u_2]^\top$, $w = [w_{b1}, w_{b2}, w_{b3}, w_w]^\top$, and $v = [v_x, v_y, v_\psi, v_{U_w}]^\top$. The discrete extended Kalman filter is briefly described here, while a detailed description can be found in Brown and Hwang.[36] At every time step, the prediction, correction, and propagation processes are executed.

- **Initialization**:

$$\hat{x}_{0|0} = \hat{x}_0, \qquad P_{0|0} = \hat{P}_0, \tag{9}$$

where $\hat{x}_0$ and $\hat{P}_0$ are initial guesses of $x(t_0)$ and the covariance matrix var($x(t_0)$), with $\hat{P}_0$ normally chosen as a symmetric, positive definite matrix. The hat (ˆ) denotes the estimate.

- **Prediction**:

$$\hat{x}_{k|k-1} = f(\hat{x}_{k-1|k-1}, u(t_{k-1})), \tag{10}$$

$$P_{k|k-1} = F_{k-1} P_{k-1|k-1} F_{k-1}^\top + Q, \tag{11}$$

- **Correction**:

$$K_k = P_{k|k-1} H^\top (H P_{k|k-1} H^\top + \Upsilon)^{-1}, \tag{12}$$

$$\hat{x}_{k|k} = \hat{x}_{k|k-1} + K_k(z_k - H\hat{x}_{k|k-1}), \tag{13}$$

$$P_{k|k} = (I - K_k H) P_{k|k-1} (I - K_k H)^\top + K_k \Upsilon K_k^\top, \tag{14}$$

- **Propagation**:

$$\hat{x}_{k+1|k} = \hat{x}_{k|k-1} + hf(\hat{x}_{k|k}, u(t_k)) \tag{15}$$

$$P_{k+1|k} = \Phi_k P_{k|k} \Phi_k^\top + \Gamma Q \Gamma^\top, \tag{16}$$

where $Q \in \mathbb{R}^{3\times3}$ and $\Upsilon \in \mathbb{R}^{4\times4}$ are constant diagonal tuning matrices, corresponding to w and v, and

$$F_k = \frac{\partial f}{\partial x}\bigg|_{x=\hat{x}_{k|k}, u=u(t_k)}, \qquad \Phi_k = I + h\frac{\partial f}{\partial x}\bigg|_{x=\hat{x}_{k|k}, u=u(t_k)}, \qquad \Gamma = hE. \tag{17}$$

The Jacobian matrix $\partial f/\partial x$ used to handle the nonlinearities that exist in the process dynamics and the measurements is given in Appendix A.

3.3 | State feedback control

The nonlinear system is transformed into a linear system through feedback linearization. The nonlinearity in the model is canceled, and classical PID control algorithms can be applied. The simplified system possesses three decoupled DOFs and two control inputs, and it is hence an underactuated system. In other words, fewer DOFs than those of interest (surge, sway, and yaw) can be controlled independently.

The error vector between the current and desired position and orientation is defined as $\tilde{\boldsymbol{\eta}} = \boldsymbol{\eta} - \boldsymbol{\eta}_d$, where $\boldsymbol{\eta}_d \in \mathbb{R}^3$ is the desired position and orientation. To overcome the underactation problem, we consider to control the blade root motion in the inflow direction and the yaw angle. Hence, the error vector of the considered states is $\boldsymbol{L}\tilde{\boldsymbol{\eta}}$, where the projection matrix is $\boldsymbol{L} = \begin{bmatrix} 1 & 0 & 0 \\ 0 & 0 & 1 \end{bmatrix}$. The relative degree for the system proposed in Equation 1 is 2. Time derivative of $\tilde{\boldsymbol{\eta}}$ is $\dot{\tilde{\boldsymbol{\eta}}} = \boldsymbol{R}\boldsymbol{v} - \dot{\boldsymbol{\eta}}_d$. The model is further transformed into the reduced form with only the controlled states by multiplying by $\boldsymbol{L}$ on both sides of $\ddot{\tilde{\boldsymbol{\eta}}}$, that is,

$$\boldsymbol{L}\ddot{\tilde{\boldsymbol{\eta}}} = \boldsymbol{L}\left[\dot{\boldsymbol{R}}\boldsymbol{v} + \boldsymbol{R}\boldsymbol{M}^{-1}(\boldsymbol{R}^\top(\boldsymbol{g}+\boldsymbol{b}) + \boldsymbol{\tau}_w) - \ddot{\boldsymbol{\eta}}_d \right] + \boldsymbol{L}\boldsymbol{R}\boldsymbol{M}^{-1}\boldsymbol{R}^\top\boldsymbol{B}\boldsymbol{u}. \tag{18}$$

When Equation 3 is substituted into (18), the control input can be simplified as

$$\boldsymbol{u} = -(\boldsymbol{L}\boldsymbol{M}^{-1}\boldsymbol{B})^{-1}\left[\boldsymbol{L}\left(\boldsymbol{R}\boldsymbol{S}(r)\boldsymbol{v} + \boldsymbol{M}^{-1}(\boldsymbol{g}+\boldsymbol{b}) + \boldsymbol{R}\boldsymbol{M}^{-1}\boldsymbol{\tau}_w - \ddot{\boldsymbol{\eta}}_d \right) - \boldsymbol{u}_{pid} \right], \tag{19}$$

where $\boldsymbol{u}_{pid} = -\boldsymbol{K}_p\boldsymbol{L}\tilde{\boldsymbol{\eta}} - \boldsymbol{K}_d\boldsymbol{L}\dot{\tilde{\boldsymbol{\eta}}} - \boldsymbol{K}_i \int \boldsymbol{L}\tilde{\boldsymbol{\eta}}dt$.

Furthermore, substituting the feedback linearization control law (19) into (18) gives

$$\boldsymbol{L}\ddot{\tilde{\boldsymbol{\eta}}} = -\boldsymbol{K}_p\boldsymbol{L}\tilde{\boldsymbol{\eta}} - \boldsymbol{K}_d\boldsymbol{L}\dot{\tilde{\boldsymbol{\eta}}} - \boldsymbol{K}_i \int \boldsymbol{L}\tilde{\boldsymbol{\eta}}dt. \tag{20}$$

Defining $\boldsymbol{\zeta} = \int \boldsymbol{L}\tilde{\boldsymbol{\eta}}dt$, applying a Laplace transformation to Equation 20, and using the pole placement technique yields

$$(s^3 + \boldsymbol{K}_d s^2 + \boldsymbol{K}_p s + \boldsymbol{K}_i)\boldsymbol{\zeta}(s) = (s + \Lambda)^3 \boldsymbol{\zeta}(s) = 0, \tag{21}$$

where $\Lambda = \text{diag}(\lambda_x, \lambda_\psi)$. When the eigenvalues $-\lambda_x < 0$ and $-\lambda_\psi < 0$, the system achieves global exponential stability. By placing the poles on the negative real axis, the system is exponentially decaying without oscillation. For a second-order system with integration, placing both the two poles at the same point on negative real axis ensure a critical damping characteristic. All the three poles are selected with the same value. Hence, the PID gain matrices are found by

$$\boldsymbol{K}_p = \text{diag}\left(3\lambda_x, 3\lambda_\psi\right), \tag{22}$$

$$\boldsymbol{K}_d = \text{diag}\left(3\lambda_x^2, 3\lambda_\psi^2\right), \tag{23}$$

$$\boldsymbol{K}_i = \text{diag}\left(\lambda_x^3, \lambda_\psi^3\right). \tag{24}$$

The eigenvalues $(-\lambda_x, -\lambda_\psi)$ should be selected based on hardware capacity and the desired reaction speed. With increasing $|\lambda_x|$ and $|\lambda_\psi|$, the reaction speeds become higher, and the maximum error is smaller, but more powerful actuators are needed. Also, noise/uncertainties in the feedforward and cancellation terms in Equation 19 may be significantly amplified, severely reducing the closed-loop performance at high gains. According to the control law, the feedforward terms in Equation 19 compensating $\boldsymbol{g}$, $\boldsymbol{\tau}_w$, and $\boldsymbol{b}$, accelerate the integral controller and improve the overall performance.

3.4 | Reference model

The reference model is used to generate real-time trajectories $\boldsymbol{\eta}_d(t)$ and $\boldsymbol{v}_d(t) = \dot{\boldsymbol{\eta}}_d(t)$ to the controller, including the blade COG position, orientation, and velocity. In this paper, the final setpoint position is where the blade is stabilized and the orientation vector is denoted by $\boldsymbol{r}_d \in \mathbb{R}^2 \times \mathbb{S}$. Continuous and smooth trajectories are planned between the initial and final values to achieve a smooth control toward the final desired position and orientation. A third-order filter is adopted as the reference model, which is given by

$$\boldsymbol{\eta}_d^{(3)} + (2\Delta + \boldsymbol{I})\Omega\ddot{\boldsymbol{\eta}}_d + (2\Delta + \boldsymbol{I})\Omega^2\dot{\boldsymbol{\eta}}_d + \Omega^3\boldsymbol{\eta}_d = \Omega^3\boldsymbol{r}_d, \tag{25}$$

where $\Delta = \text{diag}\{\zeta_1, \zeta_2\} = \text{diag}\{1, 1\}$ and $\Omega = \text{diag}\{\omega_{n1}, \omega_{n2}\}$ are the matrices of relative damping ratios and natural frequencies, respectively. The parameters ω_{n1} and ω_{n2} should be tuned feasibly to the dynamic model.

4 | SIMULATION RESULTS

4.1 | Overview

Numerical simulations were conducted in the MATLAB/Simulink environment. First, the 3DOF CDM was used to tune the parameters for the observer and controller. Then, the SVM was used to verify the control scheme in detail. Selected properties of the blade installation model and the controller parameters are summarized in Table 2. The blade of the NREL 5 megawatt (MW) reference wind turbine[37] is used.

Table 3 lists the four load cases considered, with the turbulence intensities (TIs) calculated according to the IEC standard.[38] HAWC2 was used to generate the wind turbulence box according to Mann's turbulence model.[39] From the start of the simulations in MATLAB/Simulink, the wind

TABLE 2 Parameters used for numerical simulations

Parameters	Unit	Value
Position of the crane tip	m	$[0, 0, -110]^{\mathsf{T}}$
Hook mass m_h	ton	1
Yoke mass m_y	ton	50
Blade mass m_b	ton	17.74
Blade moment of inertia about COG I_b	kg/m	4.31e6
Blade length	m	62.5
Blade root center position in the body-fixed frame $\{B\}$	m	$[-0.089, -20.51, 0.145]^{\mathsf{T}}$
Position of the sling connection points in $\{B\}$	m	$[0.089, \pm 4.5, 1.855]^{\mathsf{T}}$
Length of lift wire	m	9.2
Stiffness of lift wire	N/m	5.59e8
Length of slings	m	9.0
Stiffness of slings	N/m	1e8
Lift wire and spring damping ratio	-	1%
Position of the tugger line connection points in $\{B\}$	m	$[0.089, \pm 4.5, -0.145]^{\mathsf{T}}$
Tugger line length l_t	m	10
Stiffness of the tugger lines	N/m	1e8
Noise power in the position and orientation	W/Hz	1e-8
Noise power in the wind speed sensor	W/Hz	0.005
Sensor sampling rate	Hz	100
Gain of the lowpass filter T_{iu}	-	5
Diagonal matrix T_b	-	diag($[5e6, 1e5, 2e5]$)
Constant T_w	-	100
Tuning matrix Q	-	diag($[1, 1, 1, 1]$)
Tuning matrix Υ	-	diag($[1e-9, 1e-10, 1e-12, 0.005]$)
Eigenvalues of the PID controller $[\lambda_x, \lambda_\psi]$	-	$[1, 1]$

TABLE 3 Load cases under turbulent wind conditions (Wind Turbine Class C)[38]

Load Case	1	2	3	4
Mean wind speed (U_w) (m/s)	6	8	10	12
Turbulence intensity (TI)	0.202	0.174	0.157	0.146

turbulence box moves in the positive global x-direction, and it passes the blade installation model. For each wind speed, five simulations were conducted using different random seed numbers to reduce statistical uncertainties. The seed numbers are 25, 48, 94, 242, and 596. Each simulation lasted 1000 seconds. In the response statistics, the first 400 seconds were removed during postprocessing to avoid the start-up transient effect. In the figures presented in Section 4.2, the legend "Real" denotes the simulated values without any sensor noises, the legend "Measured" stands for the simulated values with sensor noises considered, and the legend "Estimated" refers to the values estimated by the observer which filters the sensor noises.

4.2 | Observer and controller performance

4.2.1 | Control design model

The CDM is first adopted to verify the control scheme. The load case with $U_w = 10$ m/s and $TI = 0.157$ is selected as a representative case. The observer and controller performance are presented in Figure 6A-D. The results show that the controller and the observer work well for the CDM, as expected. The EKF is able to provide satisfactory estimates of the blade velocities and the wind velocity. The noise in the wind speed measurement has been filtered. Because of the effect of the tugger line force control, the range of the blade motion in the x-direction remains below 0.01 m, and the angular oscillation of the yaw motion is less than 10^{-3} deg. The tugger line force inputs u_1 and u_2 from the controller are positive, and their change rates (time derivatives) are acceptable (<20.2 kN/s). Although the blade motion in the spanwise direction is not controlled, the v-displacement is limited. This observation is consistent with the cross-flow principle, which neglects the wind speed component in the y^b-direction during the wind load calculation.
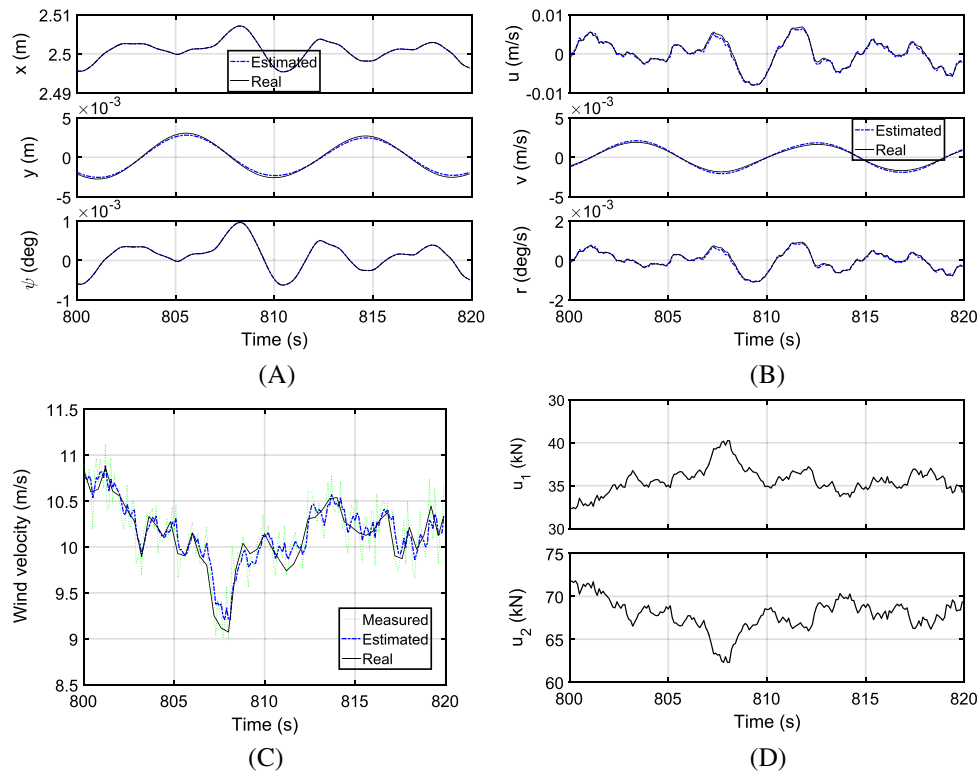
FIGURE 6 Performance of the EKF estimation for the simplified blade model, U_w=10 m/s, TI=0.157. A, Blade COG position and orientation estimation in the global frame; B, velocity estimation at the blade COG in the body-fixed frame; C, wind speed estimation in the global x-direction; and D, control inputs to the tugger lines [Colour figure can be viewed at wileyonlinelibrary.com]

4.2.2 | Simulation verification model

The SVM is used to test more realistically the performance of the proposed control and observer algorithms. The simulation results for the load case with U_w ramp up from 0 to 12 m/s in 100-300 seconds are presented in Figure 7. For the SVM, the discrepancies between the estimated and real blade motions and velocities are, as expected, greater than those for the CDM; see Figure 7A,B. However, the dynamic part of the blade oscillations in the global x-axis has been effectively maintained at less than 0.1 m because of the active force control. For the estimated wind speed, there is also a noticeable difference compared with the real wind speed, as shown in Figure 7C. Due to the spatial variation of the wind field, measurements from one location of the anemometer are not adequate for fully describing the wind speed variation along the blade, and the wind speed estimate therefore deviates. It is also seen to be somewhat noisy. Although the wind speed estimate is not accurate, it can still be used to accelerate the disturbance rejection part of the controller and reduce the initial drift, since the mean estimated wind speed approximately tracks the actual wind speed. Similar to the observation of the CDM, the tugger line forces are always positive during the simulations, and the change rates are still within reasonable ranges (<7.25 kN/s). The change rates is smaller than those in Section 4.2.1 because of the actuator lowpass dynamics.

4.3 | Comparison of active and passive schemes

4.3.1 | Time histories

A set of comparative studies of the active control scheme with a typical passive single blade installation system were conducted to evaluate the performance the proposed controller under various wind conditions. The passive system has the same structural properties as the SVM, but the tugger lines are not actively controlled.

The time-domain results are compared in Figure 8 for the selected load case. For the passive system (dash-dot line in the figure), the blade surge motion in the x-direction is dominant, and the motion maxima is within 2 m in this case, where motion maxima is defined by the difference between the motion response maxima and its mean value. Compared with the blade surge motion, the sway and heave motions in the y- and z-directions are small, with the absolute motion maxima below 0.2 m.

In contrast, when the active scheme is applied, the blade surge motion in the x-direction has a significant reduction. For the blade sway and heave motions in the y- and z-directions, the response magnitudes are slightly reduced compared with those of the passive system. This result is reasonable because the y- and z- motions are not controlled. In addition, the blade root sway motion is also affected by the controlled yaw motion, which is further related to the controlled surge motion. Although the active control scheme is mainly effective in the x-direction, it thus also reduces the motions of the other DOFs.
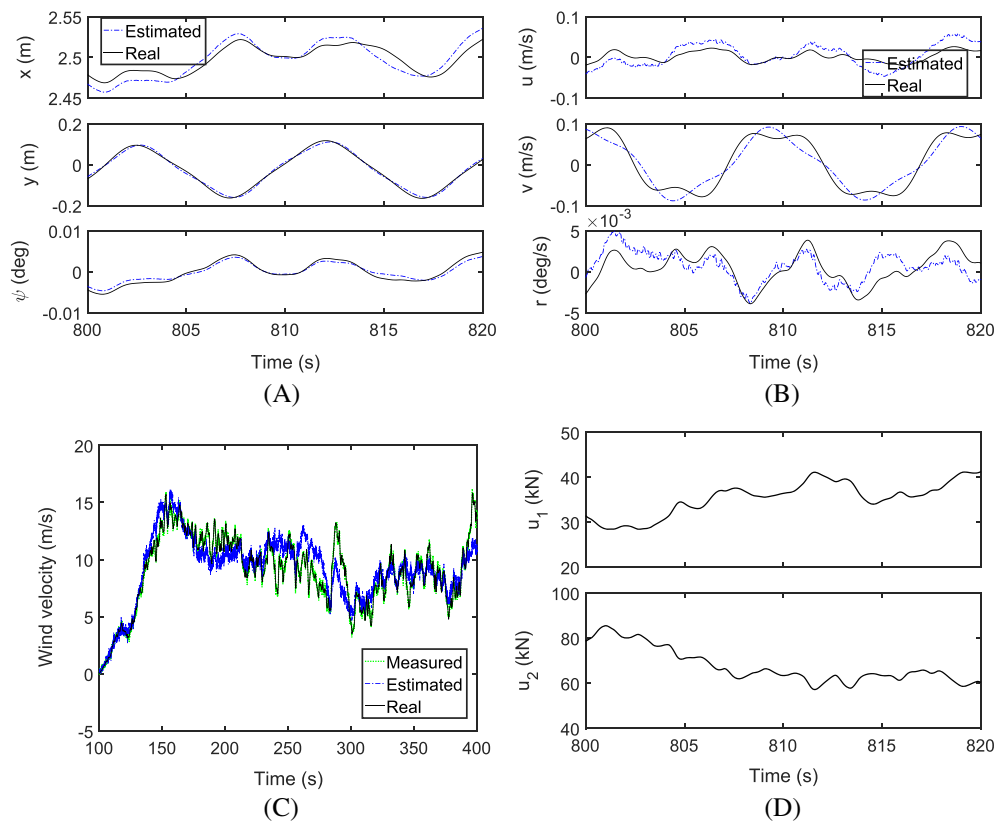
FIGURE 7 Performance of the EKF estimation at the blade COG for the SVM, U_w=10 m/s and TI=0.157. A, Blade COG position and orientation estimation in the global frame; B, velocity estimation at the blade COG in the body-fixed frame; C, wind speed estimation in the global x-direction; and D, control inputs to the tugger lines [Colour figure can be viewed at wileyonlinelibrary.com]
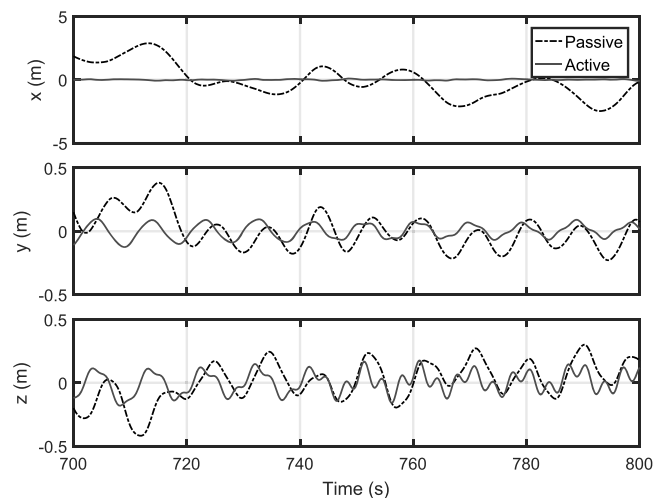
FIGURE 8 Time histories of the blade root center displacement relative to the mean position using the SVM, U_w = 10 m/s and TI = 0.157

4.3.2 | Statistical results

The statistics were obtained by averaging the results of five 600-second simulations. The standard deviation and the motion maxima are used as the main criteria for evaluating the effect of active control. The mean value is always controlled accurately to the constant reference value.

As shown in Figure 9, the motion maxima in the x-direction is dominant, and the use of active control causes a significant reduction for both the blade COG and root center. Under the investigated mean wind speeds from 6 to 12 m/s, the maximum reduction exceeds 90%. Reductions are also observed in the y- and z-directions, albeit less prominent because of coupling with other DOFs. When the blade yaws about the z-axis, the rotational center is close to the COG. Hence, the motion in one DOF of the blade root is more affected by other DOFs because of rigid body motions. For example, the sway motion of the blade root center is more influenced than the blade COG by the yaw motion.

FIGURE 9 Motion maxima of the blade-root center and the blade COG using the SVM; $U_w = 6 - 12$ m/s, average of five 600-second simulations

FIGURE 10 Standard deviation of the motions at the blade root center and the blade COG using the SVM; $U_w = 6 - 12$ m/s, average of five 600-second simulations

Figure 10 compares the standard deviations of the response for the passive and the active schemes. Similar to the motion maxima, the standard deviation has the greatest reduction in the *x*-direction at all wind speeds, but reductions are also observed in the *y*- and *z*-directions.
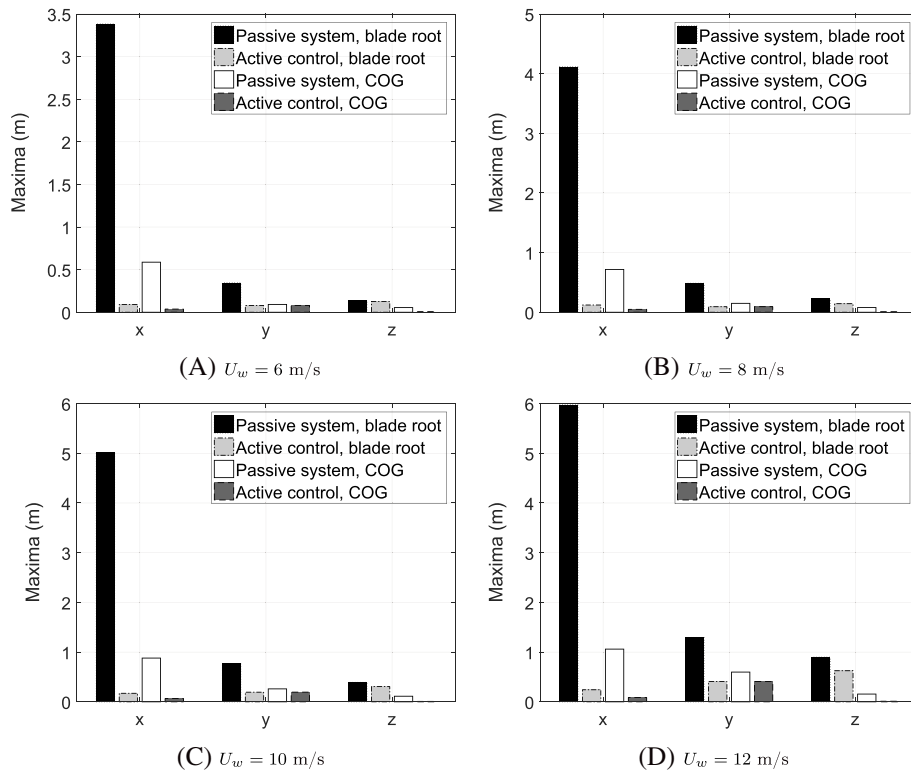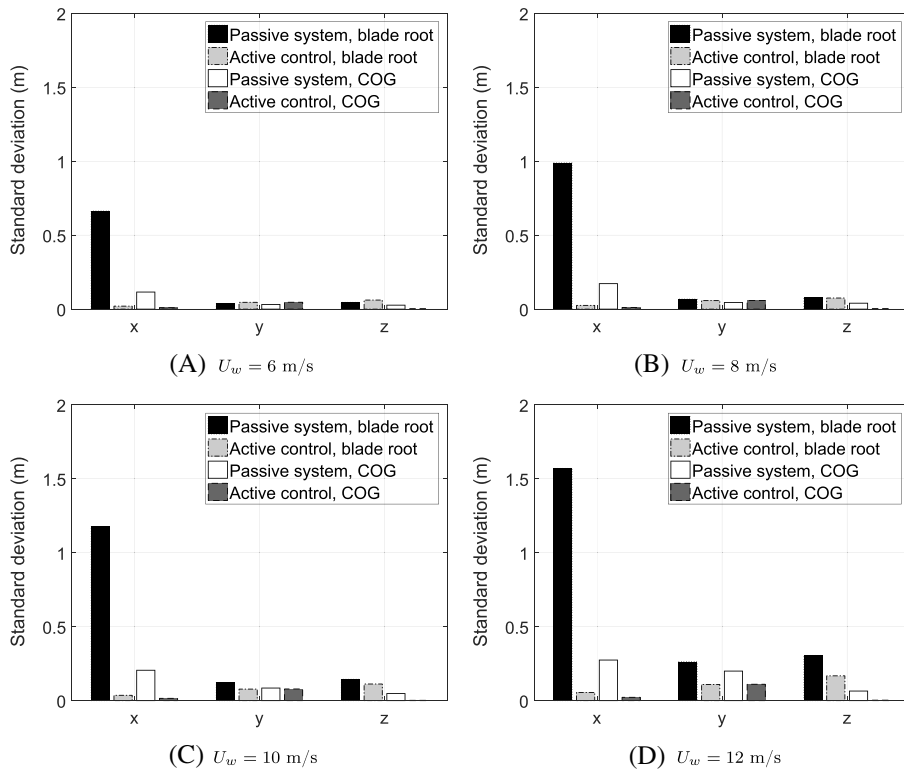
Overall, the statistical results are consistent with the time series of blade root motions. In the blade mating process, the blade root will be docked into the hub, and the blade root motions in the *xz*-plane are closely associated with the success rate of the mating process. The proposed control system considerably reduces the motion variations in the *x*-direction and indicates a potential for improved mating efficiency.

5 | CONCLUSIONS AND FUTURE WORK

This paper proposes a closed-loop scheme for active tugger line force control for single blade installation. To facilitate the design of the observer algorithm and control law, the blade installation system was simplified as a 3DOF control design model. Based on the reduced model, an extended Kalman filter, a state feedback linearization and feedforward compensation algorithm, and pole placement techniques were applied to design the proportional-integral-derivative controller. A third-order reference model was adopted to provide smooth position and velocity trajectories in real time. In addition to the control design model, a simulation verification model that includes a 6DOF blade, other lifting components, and more realistic environmental load models was also developed. To verify the performance of the control system, time-domain simulations were conducted in turbulent wind conditions.

It was found that the proposed actively-controlled tugger line system works well as tested with the simulation verification model. A comparison with a passive system without control shows that the active control scheme can effectively reduce the blade-root surge motion standard and maxima deviations. This observation indicates that the active tugger line control method can potentially expedite the blade mating process.

In future work, other scenarios of single blade installation is planned to be addressed. For example, flexibility of the crane tip should be considered for the boundary condition of the lift wire, and other possible directions of the tension provided by the tugger lines should also be considered. In addition to the blade-root motions, the monopile vibrations may also cause concern during the blade mating process. Thus, real-time measurement of the monopile vibrations from available sensors, such as inertial measurement units (which steadily become better and cheaper), may be used by the controller. For accurate representation of the aerodynamic loading on large wind turbine blades during installation, structural flexibility and advanced computational methods such as the computational fluid dynamics method can be considered.

ORCID

Zhengru Ren http://orcid.org/0000-0001-5522-8094
Zhiyu Jiang http://orcid.org/0000-0002-8778-0999
Roger Skjetne http://orcid.org/0000-0001-9289-1450

REFERENCES

1. Commission of the European Communities. *Communication From the Commission to the European Parliament, the Council, the European Economic and Social Committee and the Committee of the Regions—offshore wind energy: Action Needed to Deliver on the Energy Policy Objectives for 2020 and Beyond.* The European Commission; 2008.

2. WindEurope. Wind in power: 2016 European statistics; 2017.

3. Soyoz S, Aydin C. Effects of higher wave harmonics on the response of monopile type offshore wind turbines. *Wind Energy*. 2013;16(8):1277-1286.

4. Pahn T, Rolfes R, Jonkman J. Inverse load calculation procedure for offshore wind turbines and application to a 5-mw wind turbine support structure. *Wind Energy*. 2017;20(7):1171-1186.

5. Shirzadeh R, Weijtjens W, Guillaume P, Devriendt C. The dynamics of an offshore wind turbine in parked conditions: a comparison between simulations and measurements. *Wind Energy*. 2015;18(10):1685-1702.

6. Zhang D, Yue Q. Major challenges of offshore platforms design for shallow water oil and gas field in moderate ice conditions. *Ocean Eng*. 2011;38(10):1220-1224.

7. Shi W, Park HC, Na S, Song J, Ma S, Kim CW. Dynamic analysis of three-dimensional drivetrain system of wind turbine. *Int J Precis Eng Manuf*. 2014;15(7):1351-1357.

8. Moné C, Hand M, Bolinger M, Rand J, Heimiller D, Ho J. 2015 cost of wind energy review; 2017.

9. Kaiser MJ, Snyder B. Offshore wind energy installation and decommissioning cost estimation in the U.S. outer continental shelf. In: Energy Research Group LLC. Louisiana, Baton Rouge; 2010.

10. Gaunaa M, Bergami L, Guntur S, Zahle F. First-order aerodynamic and aeroelastic behavior of a single-blade installation setup. *J Phys: Conf Ser*. 2014;524(1):012073.

11. Gaunaa M, Heinz J, Skrzypiński W. Toward an engineering model for the aerodynamic forces acting on wind turbine blades in quasisteady standstill and blade installation situations. *J Phys Conf Ser*. 2016;753(2):022007.

12. Skrzypiński W, Gaunaa M, Heinz J. Modelling of vortex-induced loading on a single-blade installation setup. *J Phys: Conf Ser*. 2016;753(8):082037.

13. Kuijken L. Single blade installation for large wind turbines in extreme wind conditions. *Master's Thesis*; 2015.

14. Jiang Z, Gao Z, Ren Z, Li Y, Duan L. A parametric study on the blade mating process for monopile wind turbine installations under rough environmental conditions. *Eng Struct*. 2018;172:1042-1056.

15. Liftra. LT575 Blade Dragon. http://liftra.com/product/blade-dragon/. Accessed August 10, 2017.

16. HighWind. The boom lock. http://www.high-wind.eu/boomlock/. Accessed August 10, 2017.

17. Fang Y, Wang P, Sun N, Zhang Y. Dynamics analysis and nonlinear control of an offshore boom crane. *IEEE Trans Ind Electron*. 2014;61(1):414-427.

18. Ngo QH, Hong K-S. Sliding-mode antisway control of an offshore container crane. *IEEE/ASME Trans Mechatron*. 2012;17(2):201-209.

19. Masoud ZN, Nayfeh AH, Mook DT. Cargo pendulation reduction of ship-mounted cranes. *Nonlinear Dyn*. 2004;35(3):299-311.

20. Abdel-Rahman EM, Nayfeh AH, Masoud ZN. Dynamics and control of cranes: a review. *Modal Anal*. 2003;9(7):863-908.

21. Xu J, Ren Z, Li Y, Skjetne R, Halse KH. Dynamic simulation and control of an active roll reduction system using free-flooding tanks with vacuum pumps. *J Offshore Mech Arct Eng*. 2018;140(6):061302.

22. Johansen TA, Fossen TI, Sagatun SI, Nielsen FG. Wave synchronizing crane control during water entry in offshore moonpool operations-experimental results. *IEEE J Oceanic Eng*. 2003;28(4):720-728.

23. Messineo S, Celani F, Egeland O. Crane feedback control in offshore moonpool operations. *Control Eng Pract*. 2008;16(3):356-364.

24. Martínez J, Rodriguez P, Kjær PC, Teodorescu R. Design and coordination of a capacitor and on-load tap changer system for voltage control in a wind power plant of doubly fed induction generator wind turbines. *Wind Energy*. 2012;15(4):507-523.

25. Díaz de Corcuera A, Pujana-Arrese A, Ezquerra JM, Milo A, Landaluze J. Linear models-based LPV modelling and control for wind turbines. *Wind Energy*. 2015;18(7):1151-1168.

26. Lu Q, Bowyer R, Jones BL. Analysis and design of coleman transform-based individual pitch controllers for wind-turbine load reduction. *Wind Energy*. 2015;18(8):1451-1468.

27. Skjetne R, Fossen TI, Kokotović PV. Adaptive maneuvering, with experiments, for a model ship in a marine control laboratory. *Automatica*. 2005;41(2):289-298.

28. RWE Innogy GmbH. Halfway through the turbine installation for the nordsee ost offshore wind farm. 2014. [Online; Accessed July 16, 2017].

29. Ren Z, Jiang Z, Skjetne R, Gao Z. Development of a numerical simulator for offshore wind turbine blades installation. *Ocean Eng*. 2018. https://doi.org/10.1016/j.oceaneng.2018.05.011

30. Larsen TJ, Hansen AM. How 2 hawc2, the user's manual; 2007.

31. Hu W, Choi KK, Zhupanska O, Buchholz JH. Integrating variable wind load, aerodynamic, and structural analyses towards accurate fatigue life prediction in composite wind turbine blades. *Struct Multi Optim*. 2016;53(3):375-394.

32. Liang H, Chen X. A new multi-domain method based on an analytical control surface for linear and second-order mean drift wave loads on floating bodies. *J Comput Phys*. 2017;347:506-532.

33. Egeland O, Gravdahl JT. *Modeling and Simulation for Automatic Control*. Norway: Marine Cybernetics Trondheim; 2002.

34. Bø TI, Dahl AR, Johansen TA, et al. Marine vessel and power plant system simulator. *IEEE Access*. 2015;3:2065-2079.

35. Loria A, Fossen TI, Panteley E. A separation principle for dynamic positioning of ships: Theoretical and experimental results. *IEEE Trans Control Syst Technol*. 2000;8(2):332-343.

36. Brown RG, Hwang P YC. *Introduction to Random Signals and Applied Kalman Filtering with MATLAB Exercises*, 4th ed. Wiley; 2012.

37. Jonkman J, Butterfield S, Musial W, Scott G. Definition of a 5-mw reference wind turbine for offshore system development. Technical Report No. NREL/TP-500-38060, National Renewable Energy Laboratory, Golden, CO; 2009.

38. IEC 61400-1. *Wind Turbine Generator Systems-Part 1: Safety Requirements*. Geneva, Switzerland: International Electrotechnical Commission and others; Standard; 2005.

39. Jonkman BJ, Kilcher L. Turbsim user's guide: version 1.06; 2012.

APPENDIX A: LIST OF MATRICES

$$
H = \begin{bmatrix} 1 & 0 & 0 & 0 & 0 & 0 & 0 & 0 & 0 & 0 \\ 0 & 1 & 0 & 0 & 0 & 0 & 0 & 0 & 0 & 0 \\ 0 & 0 & 1 & 0 & 0 & 0 & 0 & 0 & 0 & 0 \\ 0 & 0 & 0 & 0 & 0 & 0 & 0 & 0 & 0 & 1 \end{bmatrix} \tag{A1}
$$

$$
E = \begin{bmatrix} 0 & 0 & 0 & 1 & 0 & 0 & 0 & 0 & 0 & 0 \\ 0 & 0 & 0 & 0 & 1 & 0 & 0 & 0 & 0 & 0 \\ 0 & 0 & 0 & 0 & 0 & 1 & 0 & 0 & 0 & 0 \\ 0 & 0 & 0 & 0 & 0 & 0 & 0 & 0 & 0 & 1 \end{bmatrix} \tag{A2}
$$

$$
\frac{\partial \boldsymbol{f}}{\partial \boldsymbol{x}} =
\begin{bmatrix}
0 & 0 & -S_\psi u - C_\psi v & 0 & 0 & 0 & C_\psi & -S_\psi & 0 & 0 \\
0 & 0 & C_\psi u - S_\psi v & 0 & 0 & 0 & S_\psi & C_\psi & 0 & 0 \\
0 & 0 & 0 & 0 & 0 & 0 & 0 & 0 & 1 & 0 \\
0 & 0 & 0 & -\frac{1}{T_{b1}} & 0 & 0 & 0 & 0 & 0 & 0 \\
0 & 0 & 0 & 0 & -\frac{1}{T_{b2}} & 0 & 0 & 0 & 0 & 0 \\
0 & 0 & 0 & 0 & 0 & -\frac{1}{T_{b3}} & 0 & 0 & 0 & 0 \\
-\frac{g}{l}C_\psi & -\frac{g}{l}S_\psi & \frac{g}{l}(S_\psi x - C_\psi y) - \frac{2a}{m}U_w^2 C_\psi S_\psi + \frac{1}{m}(-b_1 S_\psi + b_2 C_\psi) + \frac{S_\psi}{m}(u_1 + u_2) & \frac{C_\psi}{m} & \frac{S_\psi}{m} & 0 & 0 & 0 & 0 & \frac{2a}{m}U_w C_\psi^2 \\
\frac{g}{l}S_\psi & -\frac{g}{l}C_\psi & \frac{g}{l}(-C_\psi x + S_\psi y) + \frac{1}{m}(-b_1 S_\psi - b_2 C_\psi) + \frac{C_\psi}{m}(u_1 + u_2) & -\frac{S_\psi}{m} & \frac{C_\psi}{m} & 0 & 0 & 0 & 0 & 0 \\
0 & 0 & -\frac{2b}{l}U_w^2 C_\psi S_\psi + \frac{S_\psi}{l}(r_{t1}u_1 - r_{t2}u_2) & 0 & 0 & \frac{1}{l} & 0 & 0 & 0 & \frac{2b}{l}U_w C_\psi^2 \\
0 & 0 & 0 & 0 & 0 & 0 & 0 & 0 & 0 & -\frac{1}{T_w}
\end{bmatrix}
\tag{A3}
$$